Insights into optimized synthesis conditions of hollow microspheres of silica for water vapor adsorption

Bianca Ferreira dos Santos[a], Juan Antonio Cecilia[b], Moisés Bastos-Neto[a], Enrique Rodríguez-Castellón[b], Diana Cristina Silva de Azevedo[a], Enrique Vilarrasa-García[a],*

[a] Grupo de Pesquisa em Separações por Adsorção (GPSA), Departamento de Engenharia Química, Universidade Federal do Ceará, Campus do Pici, 60455-760, Fortaleza, Ceará, Brazil
[b] Departamento de Química Inorgánica, Cristalografía y Mineralogía, Facultad de Ciencias, Universidad de Málaga, 29071, Málaga, Spain

ARTICLE INFO

ABSTRACT

Hollow microspheres of silica were synthesized with different ethanol/water ratios (0.4, 1.0, 2.0 and 6.0) to assess the influence of this parameter on the morphology/porosity of the samples and thus on their water adsorption capacity. The samples were characterized by N_2 at 77 K and CO_2 at 273 K adsorption isotherms, scanning electron microscopy, transmission electron microscopy and water vapor isotherms at 298, 313 and 328 K. The textural properties of the samples were slightly different: as the ethanol/water ratio increases, the pore volume and specific surface area decrease and the structure of the samples evolves into a well-defined spherical arrangement. In addition, water adsorption capacity of the samples was similar to that of commercial adsorbents used for gas drying at high relative pressures, but significantly lower at low relative pressures. Moreover, varying of the ethanol/water ratio did not lead to a noticeable improvement in the water adsorption capacity at low relative pressures and hence these samples are not suitable for deep gas drying. On the other hand, as they require less energy to be regenerated, HMS are alternatives to be considered in less demanding situations, such as coarse drying and water harvesting from air.

1. Introduction

Water adsorption has attracted the interest of the scientific community as a possible solution to some of the society's concerns, such as the need to use alternative energy resources or reduce global water scarcity.

Natural gas has been playing an important role in the world energy matrix, having supplied 24% of the total energy demand in 2019 (BP, 2020). Moreover, due to its low carbon content, natural gas has been considered a transition fuel from a current coal/oil dominated scenario towards a future zero-carbon energy matrix (De Guido et al., 2018; Safari et al., 2019; Gürsan and Gooyert, 2021). Raw natural gas consists mainly of methane (75–90%), ethane, propane, butane and other long-chain hydrocarbons, together with undesired species such as carbon dioxide, hydrogen sulfide, mercaptans, nitrogen, water and mercury. Hence, natural gas processing consists of several steps to meet not only pipelines specifications, but also emission limits and regulations (Baker and Lokhandwala, 2008; Mokhatab et al., 2019).

In natural gas processing, dehydration is an essential step, since the presence of water may lead to problems during transportation and processing, such as the formation of hydrates, corrosion and reduction of its calorific value. Hydrates may block pipelines and process equipment, whereas corrosion is intensified by the combination of water with acid gases, such as carbon dioxide and hydrogen sulfide. Furthermore, condensed water in pipelines may causes slug flow and erosion (Netušil and Ditl, 2012; Bahadori, 2014).

Common water content specifications imposed on natural gas are those for the liquid natural gas (LNG) feed plant (<0.1 ppmv) and

pipeline gas (<120 ppmv). Adsorption in zeolite molecular sieves is the most suitable method when strict specifications (e.g., LNG feed plant) are required and is usually performed by a cyclic process involving temperature swings (TSA) (Berg et al., 2019; Mokhatab et al., 2019). In TSA processes, water is desorbed from the adsorbent (for cyclic use) by heating, usually with a hot gas stream (Ruthven, 1984). Water will interact strongly with the adsorbent surface in microporous hydrophilic materials with high heat of adsorption, requiring more energy for the regeneration step (Berg et al., 2019).

Commonly used commercial adsorbents for natural gas drying are silica gel, activated alumina and zeolite molecular sieves. Among these adsorbents, zeolites are the adsorbent of choice when it is necessary to achieve a strict (low) content of water (<0.1 ppmv) thanks to their high-water adsorption capacity at low relative pressures. On the other hand, they are the most expensive adsorbent for this application and have the highest heats of water adsorption, requiring high temperatures (around 573 K) to be regenerated. Thus, the use of materials such as silica gel could be beneficial, since it requires lower regeneration temperatures (around 423 K), which could lead to a reduction in the process energy consumption (Mokhatab et al., 2019; Kidnay et al., 2019).

Moreover, even though the regeneration of silica-based adsorbents requires less energy, its application has an important drawback: when compared to zeolites, their water adsorption capacity at low relative pressures is considerably smaller (Oh et al., 2017; Wynnyk et al., 2019). Therefore, silica gel is usually not able to further reduce the water content of a gas below 10 ppmv (IEAGHG, 2014) and is preferably used as a primary dryer in a layered bed. Silica gel is commonly the first layer that adsorbs water, then the zeolite layer adsorbs the remaining water and ensures that the gas comes out of the column with a very low water content. In addition, the association of silica gel and zeolite could provide a longer water vapor breakthrough time in comparison with a bed that only contains zeolite (Nastaj and Ambrozek, 2015; Saadat et al., 2018).

Another aspect related to this research is the water shortage that has caused serious concerns around the globe in recent decades. There is interest in developing cheap and portable methods to guarantee the supply and access to fresh water (Lundqvist et al., 2019). Desalination, sewage recycling, wastewater treatment, and adsorption based atmospheric water harvesting (AWH) are some of the proposed methods. The high-energy consumption and inaccessibility in remote areas discourages the desalination method (Ahmed et al., 2019). Recycling and treating wastewater require infrastructure and significant capital investments. Therefore, adsorption-based atmospheric water harvesting becomes an interesting option in less densely populated water-stressed areas. Furukawa et al. (2014) reported some water adsorption capacities for MOFs, zeolites and silica considering the delivery of drinking water in arid areas such as MOF-841 adsorbing 0.442 gg^{-1}, zeolite 13X 0.309 gg^{-1} and MCM-41 0.048 gg^{-1} at P/P_0 = 0.3. Permyakova et al. (2017) modified MIL-101-Cr with $CaCl_2$ improving water adsorption capacity at P/P_0 = 0.3, reaching 0.580 gg^{-1}. However, the high affinity between water and salt (or cations present in some of these adsorbents) may lead to an increase of the regeneration temperature, which is a clear disadvantage in terms of energy consumption.

An ideal adsorbent for AWH should be stable and hydrophilic; those showing type IV and type V water isotherms are the most appropriate (LaPotin et al., 2019; Sultan et al., 2021). The water adsorption capacity should increase linearly as relative humidity increases, while in the desorption process, the amount of water retained should drop steeply with increasing temperature. Taking into account these requirements, silica-based materials can be promising adsorbents for this purpose.

Therefore, the present study aims to evaluate the use of hollow microspheres of silica (HMS) for gas drying or eventually adsorption based atmospheric water harvesting (AWH). This material was chosen because it is versatile, with tunable morphological/textural properties, which are achieved by different strategies: using swelling agents (Cecilia et al., 2016; Sousa et al., 2021) or changing reactants ratio (Hu et al., 2010), which was the strategy applied in this work. Swelling agents such as aromatic hydrocarbons act by moving into the hydrophobic core, expanding the dimensions of the surfactant micelle and, consequently, the pore size. Although this leads to enhanced diffu-

sion of large molecules, it also causes major drawbacks such as a higher synthesis cost and the use of hazardous chemicals to the environment. Other additives such as NH_4F favor hydrolysis of the silica source and limit the growth of the silica channels, but their use also poses major environmental problems. Another option is modifying the EtOH/H_2O ratio in the synthesis route. The synthesis of hollow microspheres of silica is a micellar process-driven and increasing in the co-solvent concentration favors the spherical ordering of the micelles and increases the density of silica walls. Besides, this is a cheaper and more environmentally friendly modification (Shi et al., 2015; Zhang et al., 2007). Therefore, in this work we have used the modification in the synthesis of HMS proposed by Hu et al. (2010) without the addition of swelling reagents and we have evaluated the effects of resulting morphological and textural properties on water adsorption, adding knowledge for future design of tailored hierarchical silica-based materials competitive with the currently used those zeolite-based ones.

The HMS samples were synthesized with different ratios of ethanol/water (0.4, 1.0, 2.0 and 6.0), aiming to evaluate the water vapor uptake performance and correlate it to the textural properties and morphology. To better understand the water adsorption mechanism in these samples, the Polanyi potentials and isosteric heats of adsorption were also assessed.

2. Experimental section

2.1. Materials

The chemicals used to synthesize the samples were dodecylamine (Merck, 98%), tetraethyl orthosilicate (TEOS) (Aldrich, 98%), ethanol (VWR, 96%) and deionized water. The gases employed in this work were helium (99.999%), nitrogen (99.999%) and carbon dioxide (99.8%). All gases were supplied by White Martins Praxair.

2.2. Synthesis of hollow microspheres of silica (HMS)

The synthesis of HMS was carried out following the procedure described by Hu et al. (2010) with minor modifications. These modifications consisted mainly on the non- use of ammonia. According to Stöber et al. (1968), ammonia acts as a morphological catalyst, favoring the spherical conformation at lower ethanol/water ratio (EWR). In ammonia-free synthesis, the formation of spheres must occur at higher ethanol/water ratio than that observed by Hu et al. (2010) (EWR = 1), leading us to obtain a variety of morphologies for the EWRs chosen in this work.

In a typical synthesis of HMS, 0.83 mmol of dodecylamine (DDA) was dissolved in ethanol and then water was added to the solution, obtaining a clear solution. In all syntheses, the total volume of EtOH + H_2O solution was kept constant (40 mL), modifying the EtOH/H_2O ration between 0.4 and 6. After that, 3.84 mmol of TEOS as silicon source was added under stirring for 5 min. In the next step, the gels were aged at 298 K for 10 h. The obtained gels were filtered and washed with H_2O and EtOH and then the solids were dried at 353 K overnight. Finally, the solids were calcined under a heating rate of 1 K min^{-1} until 823 K, maintaining this temperature for 6 h.

The synthesized samples were labelled as SEW_X.X ("SEW" denotes silica, ethanol and water respectively) where X.X is ethanol/water ratio (0.4, 1.0, 2.0 and 6.0). The labels of the synthesized samples are summarized in Table S1.

2.3. Characterization

2.3.1. Textural characterization

The textural properties of the samples were estimated from N_2 adsorption/desorption isotherms at 77 K using a volumetric instrument ASAP 2020 (Micromeritics Instruments, USA). Prior to the experiments, 100 mg of each sample were outgassed at 393 K under vacuum (10^{-6} bar) for 6 h. The specific surface area (S_{BET}) was determined by the Brunauer–Emmett–Teller (BET) equation (Brunauer et al., 1938); the pore volume (V_P) was estimated by the Gurvich rule applied at a relative pressure of 0.95 (Lowell et al., 2004) and the micropore volume (V_{MIC}) was determined by the Dubinin-Radushkevich equation (Dubinin and Radushkevich, 1947). The pore size distribution (PSD) of each sample was obtained from the N_2 isotherms using the NLDFT (Non-Local Density Functional Theory) model for cylindrical pores (Evans et al., 1986).

CO_2 isotherms at 273 K were measured in order to complement the data obtained from N_2 isotherms. These measurements were performed using a volumetric instrument Autosorb-iQ$_3$ (Quantachrome Instruments, USA), following the same pretreatment conditions used for N_2 isotherms. From the CO_2 isotherms, the micropore volume (V_{MIC_CO2}), average pore width (D_P) and the micropore specific surface area (S_{MIC}) using the Dubinin–Radushkevich equation were determined.

2.3.2. Scanning and transmission electron microscopy

The morphology of the synthesized samples was evaluated by scanning electron microscopy (SEM) and transmission electron microscopy (TEM). SEM micrographs were recorded using a QUANTA 450 FEG-FEI (Thermo Fisher Scientific Company), which has a resolution of 1 nm. TEM micrographs were recorded using a high-resolution Philips CCCM 200 Supertwin-DX4 microscope equipped with a digital system for image acquisition.

2.4. Water vapor equilibrium adsorption isotherms

Water vapor isotherms were obtained at 298, 313 and 328 K using an Intelligent Gravimetric Analyzer — IGA (Hiden Isochema Ltd., UK). The system is composed by a microbalance, pressure transducers and temperature controllers. The microbalance has a stability of ± 1 μg and a weighing resolution of 0.2 μg.

Water vapor was generated using deionized water placed in a vessel that was previously degassed by repeated evacuation and vapor generation cycles to eliminate any contaminants from the free gas volume. Prior to the experiments, the samples were outgassed at 393 K under vacuum (10^{-6} mbar) for 6 h. Around 50 mg sample was used in the water vapor adsorption measurements.

The saturation pressure of water was determined by the Antoine Eq. (1) and the values obtained for the different temperatures employed in work are shown in Table S2.

$$\ln (P_{sat} \ [bar]) = A - \frac{B}{T \ [K] + C} \qquad (1)$$

2.4.1. Equilibrium model for water adsorption

The model reported by Hefti et al. (2015) was used to fit the water vapor adsorption isotherms for the studied samples. Although the Hefti model was originally proposed to water adsorption isotherms on carbon materials, Goyal et al. (2020) demonstrated that this model described well experimental data of water adsorption on silica gel. This model considers that the adsorption occurs due to different contributions. The first contribution ($q_s \ (x)$) is related to the uptake of water vapor by the functional groups and successive clustering of water molecules around these sites, and the second contribution ($q_\mu \ (x)$) is related to the capillary condensation. The Hefti model for the adsorption branch is represented by Eq. (2).

$$q(x) = q_s \ (x) + q_\mu \ (x) = \frac{q_s^\infty K_s x}{(1 - K_c x)^*(1 + (K_s - K_c) x)} + \frac{q_{\mu,a}^\infty m_a K_{\mu,a} x^{m_a}}{(1 + K_{\mu,a} x^{m_a})} \qquad (2)$$

where q_s^∞ and $q_{\mu,a}^\infty$ (mmol g^{-1}) are the saturation capacities associated with adsorption on functional groups and pores, respectively, and x represents the relative pressure; K_s, K_c and $K_{\mu,a}$ (dimensionless) are equilibrium constants, whereas m_a corresponds to the number of molecules comprising a cluster.

Note that this model is not written as a function of temperature, but only in terms of relative pressure (or relative humidity). Hefti et al. (2015) assumed that the temperature dependence can be described by the variation of saturation pressure with temperature. More details and assumptions of this equilibrium model can be found in Štěpánek et al. (2000) and Hefti and Mazzotti (2014).

3. Results and discussion

3.1. Textural characterization

The nitrogen adsorption/desorption isotherms at 77 K are presented in Fig. 1(A). In general, the isotherms present a hybrid behavior with respect to types II and IV(a) according to the isotherms classification reported by IUPAC (Thommes et al., 2015). Type II isotherm is associated with macroporous adsorbents and its shape is related to the presence of multilayer adsorption, whereas type IV isotherm is associated with mesoporous adsorbents, in which the adsorption in mesopores is determined by the adsorbent–adsorbate interactions and capillary condensation; which is accompanied by hysteresis in the case of type IV(a) (Thommes et al., 2015).

This hybrid behavior is suggested because the isotherms do not reach a well-defined plateau of saturation, characteristic of type IV isotherms, and present a behavior close to a S-shaped isotherm (with exception of SEW_6.0). Furthermore, the presence of hysteresis was observed more clearly in the isotherms of the samples with ethanol/water ratio of 0.4 and 2.0, indicating that the pore width is wider than 4 nm (Sotomayor et al., 2018).

CO_2 isotherms at 273 K presented similar adsorption capacities (1–1.5 mmol g^{-1}) at 1 bar, as presented in Fig. 2.

The textural properties of the samples, determined using the N_2 and CO_2 isotherms, are shown in Table 1. The samples have different textural properties, being SEW_0.4 the sample with the largest values of specific surface area, pore volume and micropore volume, as calculated from N_2 adsorption isotherm. These results indicate that the variation of ethanol/water ratio in the synthesis leads to slight differences in the pore network of the samples.

N_2 isotherms were used to determine the pore size distributions (PSDs) of the samples, which are plotted in Fig. 1(B). Note that PSDs indicate mainly the presence of pores in a range of 2–6 nm. In addition, the sample SEW_6.0 presented a major peak centered at 2.5 nm, whereas the other samples presented two peaks, the major peak centered between 3 and 4 nm and the secondary one close to 5.5 nm. Interest-
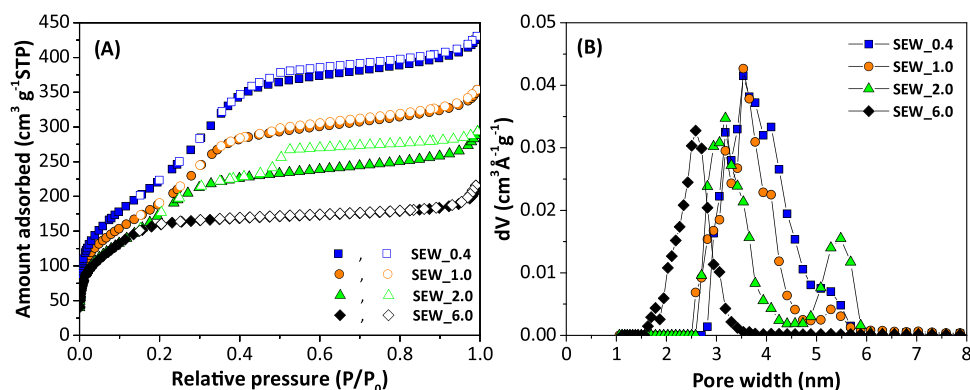
Fig. 1 – (A) N_2 adsorption/desorption isotherms at 77 K (filled symbols for adsorption branch and empty symbols for desorption branch) and (B) pore size distributions obtained by NLDFT applied to N_2 isotherms.

Table 1 – Textural properties of the samples determined from N_2 and CO_2 isotherms and particle densities.

Sample	S_{BET} (m^2 g^{-1})	V_P (cm^3 g^{-1})	$V_{MIC/N2}$ (cm^3 g^{-1})	$V_{MIC/CO2}$ (cm^3 g^{-1})	$S_{MIC/CO2}$ (m^2 g^{-1})	$D_{P/CO2}$ (nm)	Density[a] (kg m^{-3})
SEW_0.4	810	0.631	0.271	0.124	330	0.991	897
SEW_1.0	683	0.513	0.234	0.137	364	0.967	1003
SEW_2.0	601	0.411	0.191	0.135	359	1.004	1118
SEW_6.0	629	0.292	0.180	0.116	310	0.988	1273

[a] Particle density determined from pore volume (N_2 isotherm) and specific solid volume (He test).
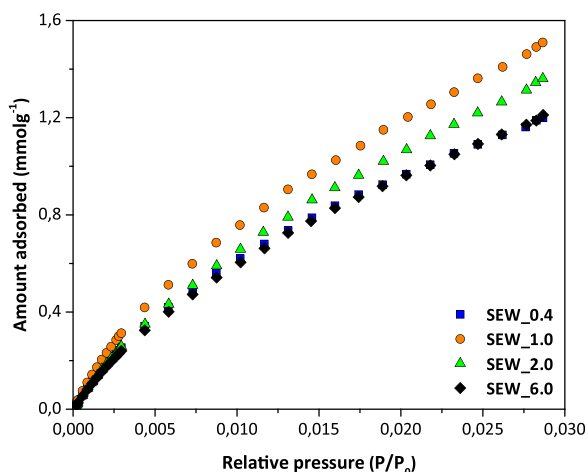

Fig. 2 – CO_2 adsorption isotherms at 273 K.

ingly, sample SEW_2.0 showed a distinct bimodal distribution as compared to samples SEW_0.4 and SEW_1.0. It is noticeable that increasing the ethanol/water ratio in the synthesis leads to HMS samples with narrower PSDs shifting towards smaller pore size range. Thus, SEW_6.0 has the most homogeneous and narrowest pore size distribution of all samples.

3.2. Scanning and transmission electron microscopy

The SEM micrographs are presented in Fig. 3 and indicate that increasing of ethanol/water ratio favors the formation of silica spheres. It could be observed that the sample synthesized with the ethanol/water ratio equals to 6.0 presents a regular spherical morphology. Increasing ethanol/water ratio leads to the isotropic growth of the silica, forming regular spheres. Firstly, it is possible to observe irregular aggregates (Figs. 3(A) and (E)) for ethanol/water ratio equals to 0.4. As the ratio increases to 1.0 and 2.0, a certain overlapping of layers occurs (Fig. 3(B) and (F)) leading to the formation of mushroom cap like structures (Fig. 3(C) and (G)), respectively. Finally, spheres formation

takes place (Fig. 3(D) and (H)) for sample synthesized with ethanol/water ratio equals to 6.0, with an enhanced particle density (Table 1).

The TEM images are presented in Fig. 4. In agreement with the SEM images, TEM also suggests progress towards a more ordered structure as the relative amount of water in the synthesis decreases. Note that at low ethanol/water ratios (EWR), samples present some agglomerates (ratio 0.4 and 1.0), which become more clumped as EWR increases (ratio 2.0) and then the spheres formation occurs (ratio 6.0). These spheres do not present a homogeneous diameter size (Fig. 4(D) and (H)), ranging between 100 and 300 nm.

In addition, it seems that the lack of morphological regularity shown by most of the samples (Figs. 3 and 4) is a drive to their pore network development (see Fig. 1(B)), since the samples synthesized with lower ethanol/water ratios are the ones with higher pore volume, wider PSD and lower density (more voids). More details of the pore structure can be observed from Small Angle X-ray Scattering diffractograms (Fig. S1) and High Resolution Transmission Electron Micrographs (Fig. S2). All samples present a major peak at about $2\theta = 1°$, which was attributed to the plane (100). This peak suggests that the samples have a uniform mesostructure (Yu et al., 2012), which is more pronounced in the sample SEW_0.4.

3.3. Water vapor isotherms

The water vapor adsorption (filled symbols) and desorption (empty symbols) data at 298 K for the samples synthesized with EWR from 0.4 to 6.0 are plotted in Fig. 5. The adsorption equilibrium isotherms are reversible and exhibit a roughly linear pattern in the low pressure range (<10 mbar), where the adsorption of water vapor takes place on silanol functional groups (Foley et al., 1997). After that, the pores are filled by clusters of water molecules that are formed around these locations, subsequently leading to capillary condensation at sufficiently large pores at higher water vapor pressure (relative pressures above 0.5). The hysteresis loop of cap-
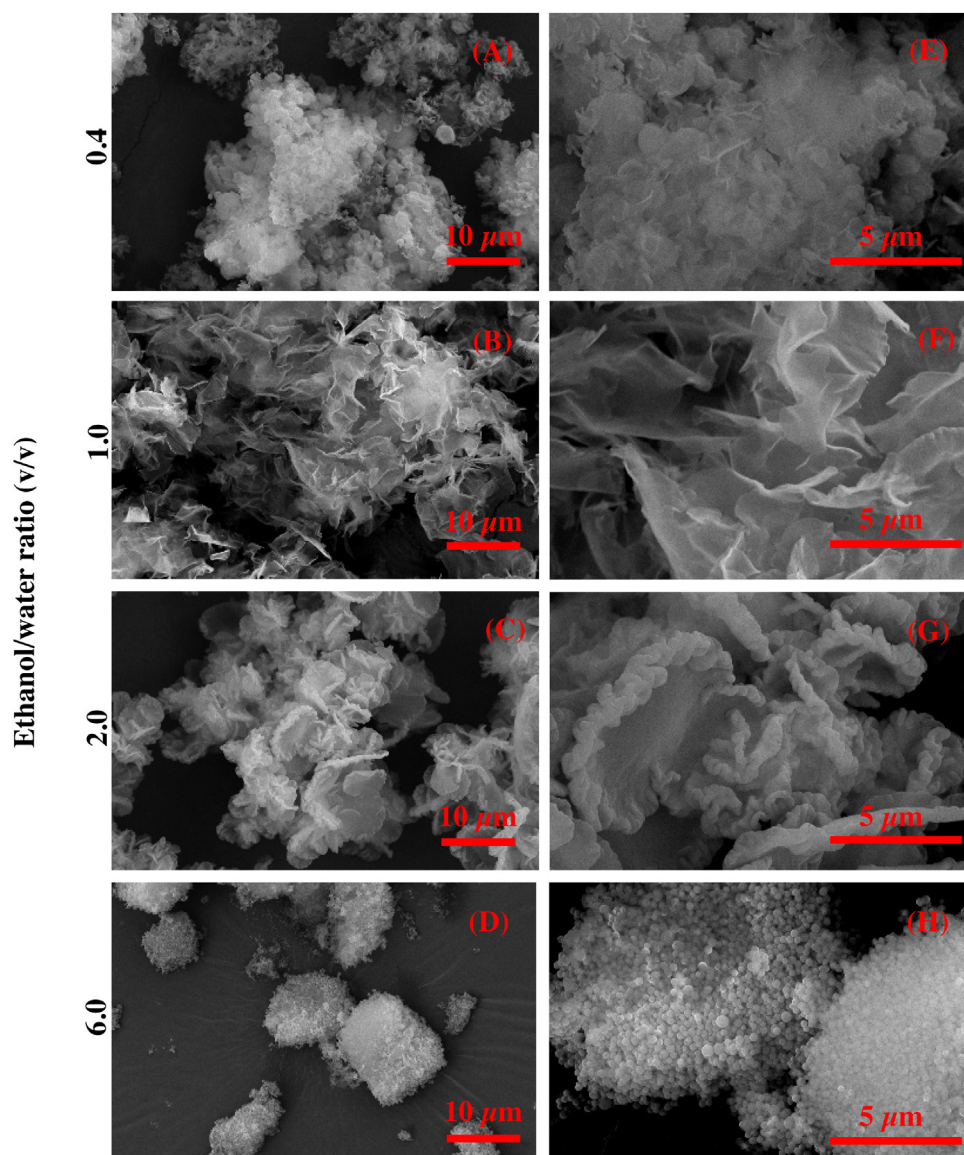
Fig. 3 – SEM images of samples synthesized with ethanol/water ratios of 0.4 (A and E), 1.0 (B and F), 2.0 (C and G), 6.0 (D and H).

Table 2 – Hefti model parameters for water vapor adsorption on SEW_0.4 and SEW_6.0.				
Sample	Parameter	298 K	313 K	328 K
SEW_0.4	$q_s^\infty \left[\mathrm{mmol\,g^{-1}}\right]$	3.72	3.86	1.13
	$K_s[-]$	11.32	8.08	63.75
	$K_c[-]$	0.87	0.76	1.16
	$q_{\mu,a}^\infty \left[\mathrm{mmol\,g^{-1}}\right]$	0.19	3.11	3.47
	$m_a[-]$	39.90	25.7	1.05
	$K_{\mu,na}[-]$	260,560	3963	0.78
	ARE [%]	2.70	5.43	0.49
SEW_6.0	$q_s^\infty \left[\mathrm{mmol\,g^{-1}}\right]$	13.46	2.80	3.34
	$K_s[-]$	2.01	14.30	11.19
	$K_c[-]$	0.0931	0.7619	0.0055
	$q_{\mu,a}^\infty \left[\mathrm{mmol\,g^{-1}}\right]$	0.10	1.91	2.24
	$m_a[-]$	22.40	4.97	4.53
	$K_{\mu,na}[-]$	536	365	139
	ARE [%]	5.97	3.16	1.54

illary condensation becomes less pronounced as the EWR increases and the pore size distribution becomes narrower so that sample SEW_6.0 does not show this effect, as observed in Fig. 6(D).

Note that the initial portion of the water isotherms (<10 mbar) is practically identical in the four samples. Considering that at low pressures the water vapor adsorption occurs mainly on sylanol groups and narrow micropores (Foley et al., 1997), the EWR seems to have a negligible effect on the con-
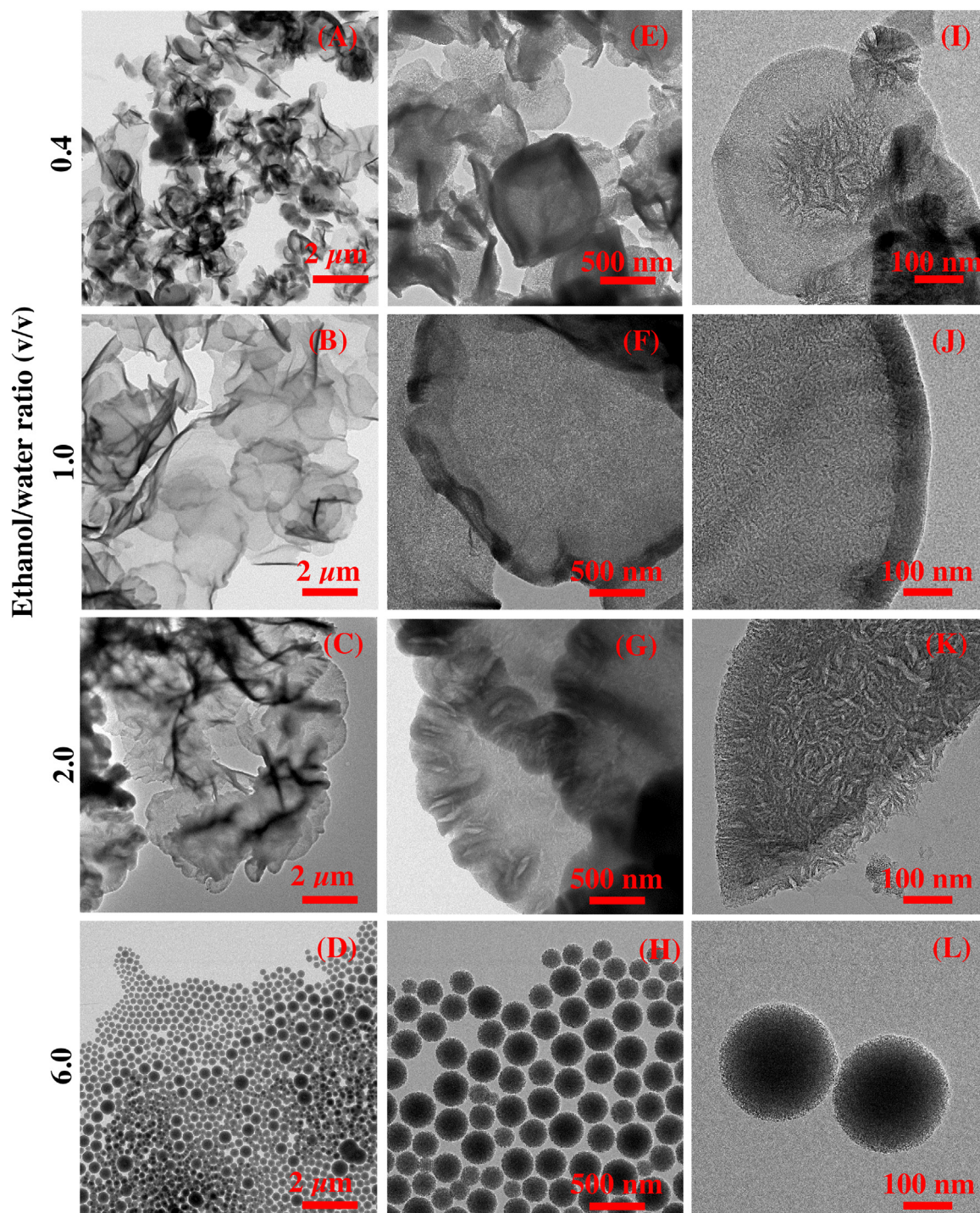
Fig. 4 – TEM images of samples synthesized with ethanol/water ratios of 0.4 (A, E, I), 1.0 (B, F, J), 2.0 (C, G, K), 6.0 (D, H, L).

centration of functional groups. Around 10 mbar, the isotherm for SEW_6.0 presents an inflection point, probably because it has the narrowest pore sizes, as observed in Fig. 1(B).

The Polanyi adsorption potential (Polanyi, 1914) was calculated according to Eq. (5) and the isotherms were plotted as a function of this potential (in Fig. 6).

$$A = RT_{ads}ln\left(\frac{1}{P/P_0}\right) \tag{5}$$

where R is the universal gas constant, T_{ads} is the temperature of the isotherm and P/P_0 is the relative pressure.

Note that the highest Polanyi potentials are observed at low coverage, as expected. The curves are coincident for all

synthesized samples until 300 kJ mol^{-1}. As the amount of adsorbed water molecules increases, the adsorption potentials decrease. This decrease does not occur in the same way for all the studied samples. For SEW_6.0, the curve shows a concave shoulder between 4 and 7 mmol g^{-1}. The shoulder decreases as the ethanol/water ratio decreases until it disappears for SEW_0.4, which has a fully convex curve. The change in the shape of the curves suggests that adsorption on these samples takes place by means of different mechanisms for intermediate to high water loadings (Sultan et al., 2015). Thus, the S-shape isotherm presented for SEW_6.0 sample is related to the filling of the pores around 2.5 nm. Sample SEW_6.0 shows the most homogeneous and narrow pore size distri-
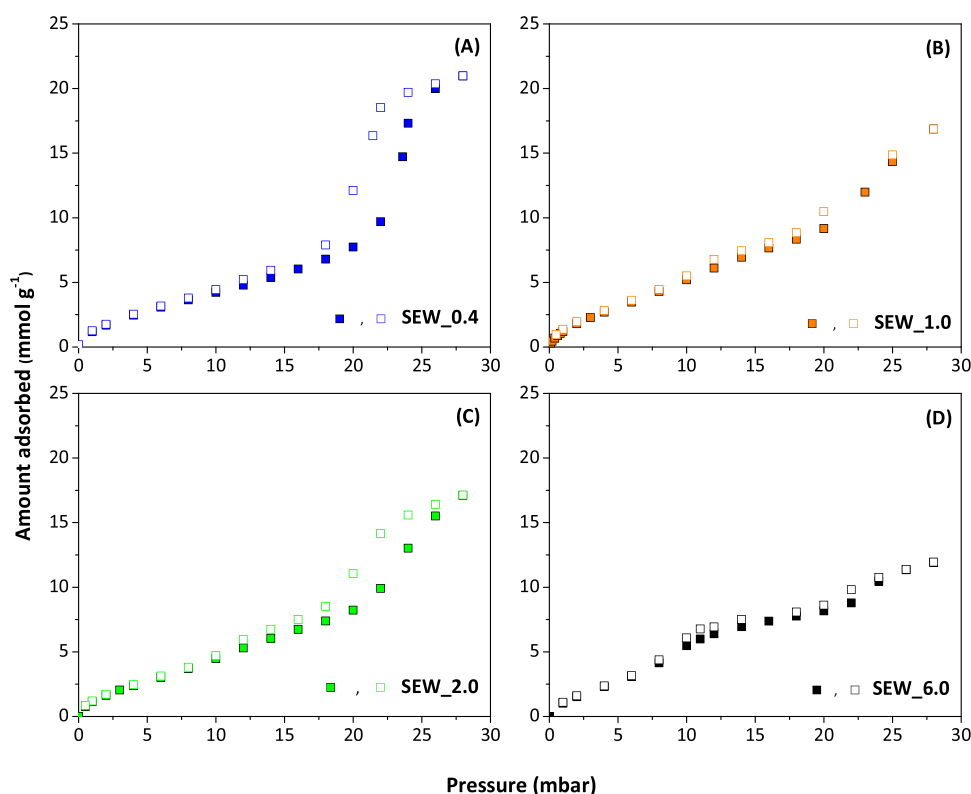
Fig. 5 – Experimental water isotherms at 298 K for synthesized samples (A) SEW_0.4, (B) SEW_1.0, (C) SEW_2.0 and (D) SEW_6.0. Filled symbols for adsorption branch and empty symbols for desorption branch.

bution of all samples. On the other hand, SEW_0.4 shows a wider pore size distribution and, for this sample, the water uptake increases linearly as P/P_0 increases. The matching of Polanyi adsorption potentials at low coverage confirm that the samples present a similar density of surface functional groups and/or similar micropore volume for the narrowest micropore sizes, as assessed by CO_2 adsorption at 273 K.

The convex curve presented by SEW 0.4 is related to the progressive filling of larger micropores and narrow mesopores, while SEW_1.0, SEW_2.0 and mainly SEW_6.0 show a shoulder in the region mentioned above, which is related to the displacement of pore size distributions to smaller pore width. Finally, for adsorption potential values lower than 50 kJ kg^{-1}, water adsorption is mainly due to capillary condensation in pores larger than 3.5−4 nm.

From this point on, the discussion will focus on the samples with EWR equal to 0.4 and 6.0. These samples were chosen because they show the most different textural properties and morphology from one another and also the least overlap in the Polanyi potential curves. The water vapor adsorption/desorption isotherms at 298, 313 e 328 K for these two samples are shown in Fig. 7, together with the Hefti model fit for the adsorption branches. Sample SEW_0.4 presents a higher water adsorption capacity than SEW_6.0 in the saturation region at 298 and 313 K. For the isotherms at 328 K, the uptakes are similar for both samples, although the experimental data are far before the saturation pressure.

Note that, as the temperature increases only 30°, the adsorption capacity drops significantly. For SEW_0.4, for example, the adsorption capacity drops from 20.97 to 2.82 mmol g^{-1} when the temperature rises from 298 to 328 K at 30 mbar. In the same conditions, the adsorption capacity of SEW_6.0 drops from 11.93 to 2.63 mmol g^{-1}. This represents reductions of

87% and 78%, respectively, suggesting that these samples can be regenerated at mild temperatures, resulting in less energy requirements in cyclic processes.

Water adsorption/desorption cycles were performed on samples SEW_0.4 and SEW_6.0 and results are shown in Fig. S3. Between adsorption steps (313 K) pressure was reduced up to 1 mbar for desorption of the previously adsorbed water molecules. Table S3 summarizes the water uptakes at each adsorption cycle. In general, the water adsorption capacity of the samples was not significantly affected over 5 cycles. Comparing the adsorption capacity in the first and fifth cycles at a relative pressure of 0.3 (∼20 mbar), variations of only 2.7 and 1.4% for SEW_0.4 and SEW_6.0 were observed, respectively. Note that porous materials have to show a high-water adsorption capacity at low relative pressures to be suitable for atmospheric water harvesting, since the relative humidity in arid regions varies between 10 and 40% (LaPotin et al., 2019). Thus, although the number of cycles was limited, results are a good indicator that SEW_0.4 and SEW_6.0 are stable samples over adsorption/desorption cycles and, consequently, show promise to be used for adsorption-based water harvesting.

Hefti model correlated well the experimental data of the adsorption branch, as shown in Fig. 7(C) for SEW_0.4 and Fig. 7(D) for SEW_6.0. Table 2 summarizes the fitting model parameters. Additionally, the average relative error (ARE) of each fitting was calculated using Eq. (3). ARE (%) values were less than 6 % and they are also presented in Table 2.

$$\mathrm{ARE} = \frac{100}{k} \sum_{j=1}^{k} \left| \frac{q_j^{exp} - q_j^{cal}}{q_j^{exp}} \right| \qquad (3)$$
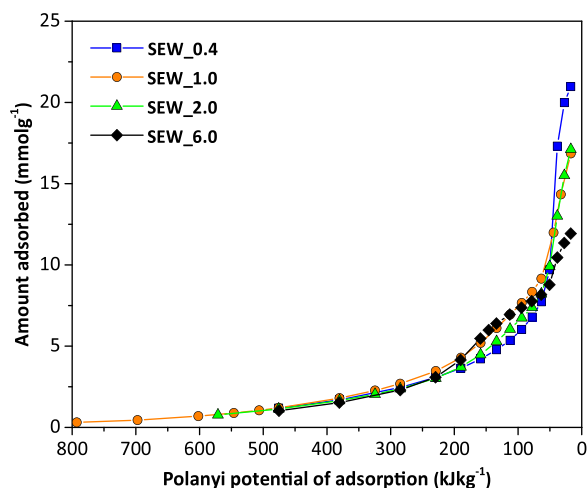
Fig. 6 – Polanyi potential of adsorption of the samples.

where k is the number of experimental points, q_j^{exp} and q_j^{cal} (mmol g^{-1}) are the experimental and calculated adsorption capacity respectively.

The water adsorption capacity of the samples at high relative pressures is comparable to values reported in the literature for commercial adsorbents, as shown in Table 3. However, the variation of ethanol/water ratio in the synthesis was not capable of improving the water adsorption capacity at low relative pressures. Thus, the synthesized samples are not recommended to stringent drying requirements.

However, as SEW_0.4 shows a high-water adsorption capacity at high relative pressures, it can be used in less strict scenarios or as primary drying agent in layered beds. Moreover, SEW_0.4, and especially SEW_6.0, show promising features for adsorption-based atmospheric water harvesting,

such as linear increase in uptake with respect to the relative pressure, a significant drop in the amount adsorbed with increasing temperature and moderate regeneration heating (Sultan et al., 2021).

The water uptake history recorded during the isotherm measurements at 298 K for SEW_0.4 and SEW_6.0 are presented in Fig. 8(A) and Fig. 8(B). The time necessary to complete the adsorption and desorption branches was similar for both samples; around 810 min and 840 min for SEW_0.4 and SEW_6.0, respectively. Although, from P/P$_0$ = 0.7 onwards the time required to complete the adsorption for SEW_0.4 is longer than for SEW_6.0, which may be related to the nucleation of water molecules in larger pores. Below P/P$_0$ = 0.7, the adsorption kinetics of the samples was not affected by the ethanol/water ratio variation.

3.3.1. Isosteric heats of water adsorption

The isosteric heat of water adsorption was estimated by the Clausius–Clapeyron equation (Rouquerol et al., 2014), according to Eq. (4).

$$Q_{st} = - \left[\frac{\partial \ln P}{\partial (1/T)} \right]_q \tag{4}$$

where Q_{st} (kJ mol^{-1}) is the isosteric heat of adsorption, P (mbar) is the equilibrium pressure and T (K) is the temperature.

The isosteric heats of adsorption are presented in Fig. 9. Note that, at low loadings, the isosteric heat of water adsorption on SEW_0.4 has a small decrease with the increase in the amount adsorbed, but it quickly reaches a constant value, as observed in Fig. 9(A). This behavior could be related to higher values of K_s and K_c parameters exhibited for SEW_0.4. These parameters according to Hefti et al. (2015) are associated with the uptake of water vapor by functional groups and narrower
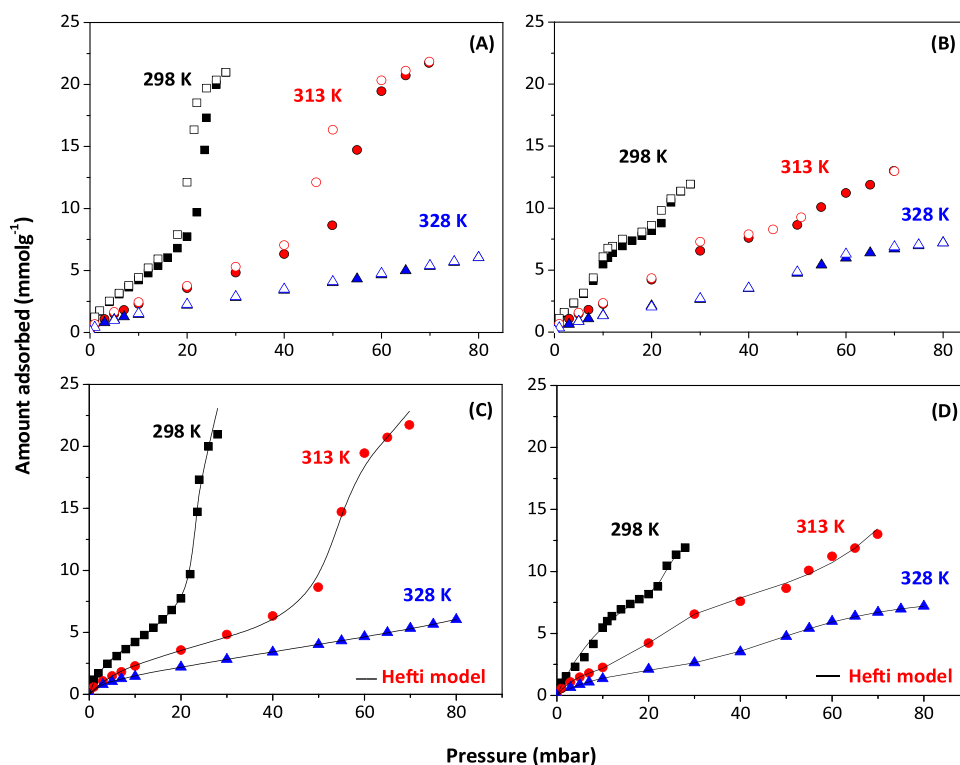

Fig. 7 – Experimental water adsorption/desorption isotherms at 298, 313 and 328 K for (A) SEW_0.4 and (B) SEW_6.0. Experimental and simulated water adsorption isotherms at 298, 313 and 328 K for (C) SEW_0.4 and (D) SEW_6.0. Filled (adsorption) and empty (desorption) symbols represent the experimental data and continuous lines are fits to the Hefti model.

Table 3 – Water vapor adsorption capacity of synthesized and commercial samples.

Sample	Water adsorption capacity (mmol g^{-1})*		Ref.
	$P/P_0 = 0.1$	$P/P_0 = 0.8$	
SEW_0.4	2.4	20.0	This work
SEW_6.0	2.3	11.4	This work
Activated alumina	8.6	17.3	Serbezov et al. (2011)
Narrow-pore silica gel	3.5	19.0	Grande et al. (2020)
Zeolite 3A (crystals)	11.2	13.0	Wang (2020)
Zeolite 4A (crystals)	13.3	14.8	Wang (2020)
Zeolite 13X (pellet)	15.9	17.6	Hefti and Mazzotti (2018)
SBA-15	0.76	29.7	Centineo et al. (2019)
Hexagonal mesoporous silica (MPS1)	0.90	9.2	Hwang et al. (2015)
MCM-41 (S12W1)	1.0	29.2	Rother et al. (2020)

* Water adsorption capacity at 298 K.
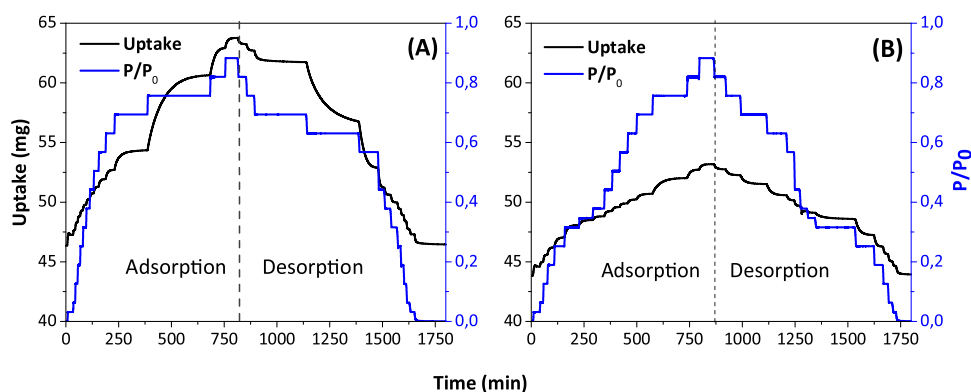
Fig. 8 – Water uptake for (A) SEW_0.4 and (B) SEW_6.0 at 298 K. Black and blue lines represent respectively water uptake and relative pressure (For interpretation of the references to color in this figure legend, the reader is referred to the web version of this article).
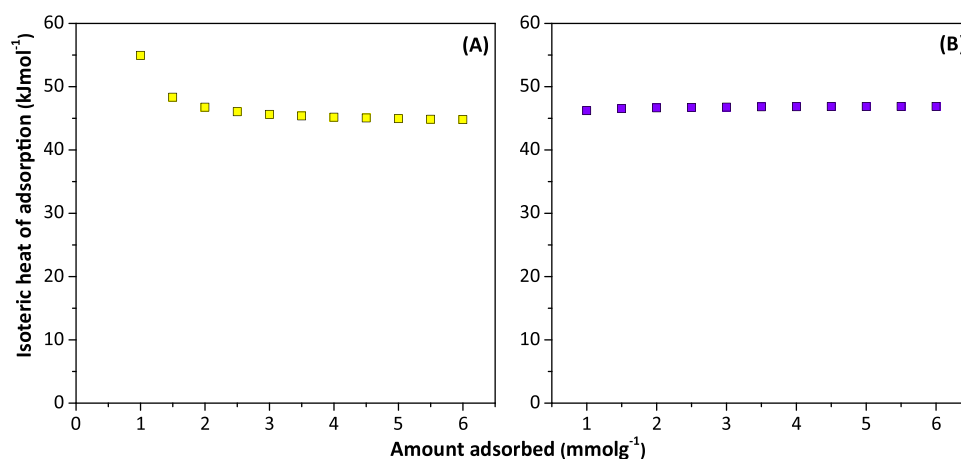
Fig. 9 – Isoteric heats of adsorption for (A) SEW_0.4 and (B) SEW_6.0.

pores and the successive gathering of water molecules around these sites. Taking into account that the textural properties in the narrower micropore region are similar for both samples, the higher values of isosteric heat of water adsorption at low coverage could be related to a slightly higher density of functional groups in SEW_0.4 than in SEW_6.0. On the other hand, the isosteric heat of water adsorption on SEW_6.0 (Fig. 9(B)) is almost constant in the entire range of amount adsorbed.

Furthermore, the average isosteric heats of adsorption were 44.79 and 46.72 kJ mol^{-1} for SEW_0.4 and SEW_6.0, respectively. These values are comparable to isosteric heats of adsorption

of commercial adsorbents commonly used for water adsorption, being closer to values reported for silica gel and activated alumina, as shown in Table S4.

4.   Conclusions

Hollow microspheres of silica have been synthesized using TEOS as silicon source and under different ethanol/water ratios (EWR) from 0.4 to 6.0. For increasing EWR, the synthesized samples presented a slight decrease in textural properties as determined by N_2 adsorption/desorption isotherms at 77 K. However, the microporosity assessed by CO_2

adsorption isotherms at 273 K did not show significant differences. In summary, the specific BET surface area and pore volume decrease from 810 to 629 m^2 g^{-1} and from 0.631 to 0.292 cm^3 g^{-1}, respectively, whereas there are no significant differences in the narrower micropore region. Additionally, the pore size distribution tends to be narrower and shift towards smaller pore sizes for samples synthesized at higher EWR. Accordingly, the structure of the samples evolves to a well-defined spherical arrangement with higher particle density as EWR increases.

Although SEW_0.4 has a less organized morphology and wider pore size distribution, this sample has the highest water adsorption capacity, probably related to the presence of larger mesopores that contribute to water condensation. Average isosteric heat of water adsorption was approximately the same irrespective the EWR, although sample SEW_0.4 showed higher enthalpy at low water loadings possibly due to more availability of silanol functional groups.

Water adsorption capacity of the samples was comparable to those of commercial drying adsorbents at high relative pressures. However, for low relative pressures HMS does not outperform zeolites and, hence, the synthesized samples are more likely to be used as a primary coarse drying agent in layered beds. Linear uptake with relative pressure and low regeneration temperature render sample SEW_0.4 – and specially SEW_6.0 – suitable characteristics for use in atmospheric water harvesting.

Declaration of interests

The authors report no declarations of interest.

Declaration of Competing Interest

The authors report no declarations of interest.

Acknowledgments

Appendix A. Supplementary data

Supplementary material related to this article can be found, in the online version, at doi:https://doi.org/10.1016/j.cherd.2021.11.020.

References

Ahmed, F.E., Hashaikeh, R., Hilal, N., 2019. Solar powered desalination—technology, energy and future outlook. Desalination 453, 54–76, http://dx.doi.org/10.1016/j.desal.2018.12.002.

Bahadori, A., 2014. Natural Gas Processing Technology and Engineering Design, 1st ed. Elsevier, pp. 441–481.

Baker, R.W., Lokhandwala, K., 2008. Natural gas processing with membranes: an overview. Ind. Eng. Chem. Res. 47, 2109–2121, http://dx.doi.org/10.1021/ie071083w.

Berg, F., Pasel, C., Eckardt, T., Bathen, D., 2019. Temperature swing adsorption in natural gas processing: a concise overview. ChemBioEng Rev. 6, 59–71, http://dx.doi.org/10.1002/cben.201900005.

BP, 2020. Statistical Review of World Energy, sixty-ninth ed, Available: https://www.bp.com/content/dam/bp/business-sites/en/global/corporate/pdfs/energy-economics/statistical-review/bp-stats-review-2020-full-report.pdf. (Accessed: May 2021).

Brunauer, S., Emmett, P.H., Teller, E., 1938. Adsorption of gases in multimolecular layers. J. Am. Chem. Soc. 60, 309–319, http://dx.doi.org/10.1021/ja01269a023.

Cecilia, J.A., Vilarrasa-Garcia, E., Garcia-Sancho, C., Saboya, R.M.A., Azevedo, D.C.S., Cavalcante Jr., C.L., Rodríguez-Castellón, E., 2016. Functionalization of hollow silica microspheres by impregnation or grafted of amine groups for the CO$_2$ capture. Int. J. Greenhouse Gas Control. 52, 344–356, http://dx.doi.org/10.1016/j.ijggc.2016.07.018.

Centineo, A., Nguyen, H.G.T., Espinal, L., Horn, J.C., Brandani, S., 2019. An experimental and modelling study of water vapour adsorption on SBA-15. Microporous Mesoporous Mater. 282, http://dx.doi.org/10.1016/j.micromeso.2019.03.018.

De Guido, G., Fogli, M.R., Pellegrini, L.A., 2018. Effect of heavy hydrocarbons on CO$_2$ removal from natural gas by low-temperature distillation. Ind. Eng. Chem. Res. 57, 7245–7256, http://dx.doi.org/10.1021/acs.iecr.8b00614.

Dubinin, M.M., Radushkevich, L.V., 1947. Equation of the characteristic curve of activated charcoal. Proceedings of the Academy of Sciences, Physical Chemistry Section USSR 55, 331–333.

Evans, R., Marconi, U.M.B., Tarzona, P., 1986. Capillary condensation and adsorption in cylindrical and slit-like pores. J. Chem. Soc. Faraday Trans. II 82, 1763, http://dx.doi.org/10.1039/F29868201763.

Foley, N.J., Thomas, K.M., Forshaw, P.L., Stanton, D., Norman, P.R., 1997. Kinetics of water vapor adsorption on activated carbon. Langmuir 13 (7), 2083–2089, http://dx.doi.org/10.1021/la960339s.

Furukawa, H., Gándara, F., Zhang, Y.-B., Jiang, J., Queen, W.L., Hudson, M.R., Yaghi, O.M., 2014. Water adsorption in porous metal–organic frameworks and related materials. J. Am. Chem. Soc. 136 (11), 4369–4381, http://dx.doi.org/10.1021/ja500330a.

Goyal, P., Purdue, M.J., Farooq, S., 2020. Adsorption and diffusion of moisture and wet flue gas on silica gel. Chem. Eng. Sci. 227, http://dx.doi.org/10.1016/j.ces.2020.115890.

Grande, C.A., Morence, D.G.B., Bouzga, M., Andreassen, K.A., 2020. Silica gel as a selective adsorbent for biogas drying and upgrading. Ind. Eng. Chem. Res. 59, 21, http://dx.doi.org/10.1021/acs.iecr.0c00949.

Gürsan, C., Gooyert, V., 2021. The systemic impact of a transition fuel: Does natural gas help or hinder the energy transition? Renew. Sustain. Energy Rev. 138, http://dx.doi.org/10.1016/j.rser.2020.110552.

Hefti, M., Mazzotti, M., 2014. Modeling water vapor adsorption/desorption cycles. Adsorption 20, 359–371, http://dx.doi.org/10.1007/s10450-013-9573-9.

Hefti, M., Mazzotti, M., 2018. Postcombustion CO$_2$ capture from wet flue gas by temperature swing adsorption. Ind. Eng. Chem. Res. 57, 15542–15555, http://dx.doi.org/10.1021/acs.iecr.8b03580.

Hefti, M., Joss, L., Marx, D., Mazzotti, M., 2015. An experimental and modeling study of the adsorption equilibrium and dynamics of water vapor on activated carbon. Ind. Eng. Chem. Res. 54, 12165–12176, http://dx.doi.org/10.1021/acs.iecr.5b03445.

Hu, J., Shan, W., Zhang, W., Zhang, Y., Tang, Y., 2010. Morphological diversity of dual meso-structured HMS and their transformation process. Microporous Mesoporous Mater. 129, 210–219, http://dx.doi.org/10.1016/j.micromeso.2009.09.017.

Hwang, J., Kataoka, S., Endo, A., Daiguji, H., 2015. Adsorption and desorption of water in two-dimensional hexagonal

mesoporous silica with different pore dimensions. J. Phys. Chem. C 119 (46), 26171–26182, http://dx.doi.org/10.1021/acs.jpcc.5b08564.

IEAGHG, 2014. Evaluation and Analysis of the Performance of Dehydration Units for CO_2 Capture, Available: https://ieaghg.org/publications/technical-reports/reports-list/9-technical-reports/991-2014-04-evaluation-and-analysis-of-the-performance-of-dehydration-units-for-co2-capture. (Accessed: June 2021).

Kidnay, A.J., Parrish, W.R., McCartney, D.G., 2019. Fundamentals of Natural Gas Processing, third ed. CRC Press, http://dx.doi.org/10.1201/9780429464942.

LaPotin, A., Kim, H., Rao, S.R., Wang, E.N., 2019. Adsorption-based atmospheric water harvesting: impact of material and component properties on system-level performance. Acc. Chem. Res. 52 (6), 1588–1597, http://dx.doi.org/10.1021/acs.accounts.9b00062.

Lowell, S., Shields, J., Thomas, M.A., Thommes, M., 2004. Characterization of porous solids and powders: surface Area. In: Porosity and Density. Springer, http://dx.doi.org/10.1007/978-1-4020-2303-3.

Lundqvist, J., Anderson, A., Johannisson, A., Lavonen, E., Mandava, G., Kylin, H., Bastviken, D., Oskarsson, A., 2019. Innovative drinking water treatment techniques reduce the disinfection-induced oxidative stress and genotoxic activity. Water Res. 155, 182–192, http://dx.doi.org/10.1016/j.watres.2019.02.052.

Mokhtab, S., Poe, W.A., Mak, J.Y., 2019. Handbook of Natural Gas Transmission and Processing: Principles and Practices, fourth ed. Elsevier, http://dx.doi.org/10.1016/C2017-0-03889-2.

Nastaj, J., Ambrozek, B., 2015. Analysis of gas dehydration in TSA system with multi-layered bed of solid adsorbents. Chem. Eng. Process. 96, 44–53, http://dx.doi.org/10.1016/j.cep.2015.08.001.

Netušil, M., Ditl, P., 2012. In: Gupta, Sreenath Borra (Ed.), Natural Gas Dehydration, Natural Gas Extraction to End Use. IntechOpen, pp. 1–22, http://dx.doi.org/10.5772/45802.

Oh, H.-T., Lim, S.-J., Kim, J.H., Lee, C.-H., 2017. Adsorption equilibria of water vapor on an alumina/zeolite 13X composite and silica gel. J. Chem. Eng. Data 62 (2), 804–811, http://dx.doi.org/10.1021/acs.jced.6b00850.

Permyakova, A., Wang, S., Courbon, E., Nouar, F., Heymans, N., D'Ans, P., Barrier, N., Billemont, P., De Weireld, G., Steunou, N., Frère, M., Serre, C., 2017. Design of salt–metal organic framework composites for seasonal heat storage applications. J. Mater. Chem. A Mater. Energy Sustain. 5, 12889–12898, http://dx.doi.org/10.1039/C7TA03069J.

Polanyi, M., 1914. Verhandl. Deutsch. Phys. Ges. 16, 1012.

Rother, G., Stack, A.G., Gautam, S., Liu, T., Cole, D.R., Busch, A., 2020. Water uptake by silica nanopores: impacts of surface hydrophilicity and pore size. J. Phys. Chem. C 124, 15188–15194, http://dx.doi.org/10.1021/acs.jpcc.0c02595.

Rouquerol, F., Rouquerol, J., Sing, K.S.W., Rouquerol, F., J. Llewellyn, P., Maurin, G., 2014. Adsorption by Powders and Porous Solids: Principles, Methodology, and Applications, second ed. Academic Press, London.

Ruthven, D.M., 1984. Principles of Adsorption and Adsorption Processes. Wiley, New York.

Saadat, S., Gholami, M., Ehsani, M.R., 2018. Mathematical modeling of adsorptive natural gas dehydration: the effect of layering the bed. Sep. Sci. Technol., 1–10, http://dx.doi.org/10.1080/01496395.2018.1543325.

Safari, A., Das, N., Langhelle, Oluf, Roy, J., Assadi, M., 2019. Natural gas: a transition fuel for sustainable system transformation? Energy Sci. Eng. 7, 1075–1094, http://dx.doi.org/10.1002/ese3.380.

Serbezov, A., Moore, J.D., Wu, Y., 2011. Adsorption equilibrium of water vapor on Selexsorb-CDX commercial activated alumina adsorbent. J. Chem. Eng. Data 56 (5), 1762–1769, http://dx.doi.org/10.1021/je100473f.

Shi, Y., Takai, C., Shirai, T., Fuji, M., 2015. Facile synthesis of hollow silica nanospheres employing anionic PMANa templates. J. Nanopart. Res. 17, 204–2013, http://dx.doi.org/10.1007/s11051-015-3010-9.

Sotomayor, F.J., Cychosz, K.A., Tommes, M., 2018. Characterization of micro/mesoporous materials by physisorption: concepts and case studies. Acc. Mater. Surf. Res. 3, 34–50.

Sousa, J.A.R., Amâncio, R., Morales-Ospino, R., Oliveira, J.L.B., Cecilia, J.A., Vilarrasa-Garcia, E., Bastos-Neto, M., Rodríguez-Castellón, Azevedo, D.S.C., 2021. H_2S and H_2O combined effect on CO_2 capture by amino functionalized hollow microsphere silicas. Ind. Eng. Chem. Res. 60, 10139–10154, http://dx.doi.org/10.1021/acs.iecr.1c00033.

Štěpánek, F., Kubíček, M., Marek, M., Šoóš, M., Rajniak, P., Yang, R.T., 2000. On the modeling of PSA cycles with hysteresis-dependent isotherms. Chem. Eng. Sci. 55, 431–440, http://dx.doi.org/10.1016/S0009-2509(99)00338-3.

Stöber, W., Fink, A., Bohn, E., 1968. Controlled growth of monodisperse silica spheres in the micron size range. J. Colloid Interface Sci. 26, 62–69, http://dx.doi.org/10.1016/0021-9797(68)90272-5.

Sultan, M., El-Sharkawy, I.I., Miyazaki, T., et al., 2015. Insights of water vapor sorption onto polymer based sorbents. Adsorption 21, 205–215, http://dx.doi.org/10.1007/s10450-015-9663-y.

Sultan, M., Bilal, M., Miyazaki, T., Sajjad, U., Ahmad, F., Chapter 2021. Adsorption-based Atmospheric Water Harvesting: Technology Fundamentals and Energy-efficient Adsorbents., http://dx.doi.org/10.5772/intechopen.97301.

Thommes, M., Kaneko, K., Neimark, A.V., Olivier, F.R.R., Rouquerol, J., Sing, S.W., 2015. Physisorption of gases, with special reference to the evaluation of surface area and pore size distribution (IUPAC Technical Report). Pure Appl. Chem. 87, 9–10, 1051–1069, http://dx.doi.org/10.1515/pac-2014-1117.

Wang, Y., 2020. Measurements and modeling of water adsorption isotherms of zeolite linde-type a crystals. Ind. Eng. Chem. Res. 59, 8304–8314, http://dx.doi.org/10.1021/acs.iecr.9b06891.

Wynnyk, K.G., Hojjati, B., Marriott, R.A., 2019. Sour gas and water adsorption on common high-pressure desiccant materials: zeolite 3A, zeolite 4A, and silica gel. J. Chem. Eng. Data 64 (7), 3156–3163, http://dx.doi.org/10.1021/acs.jced.9b00233.

Yu, J., Le, Y., Cheng, B., 2012. Fabrication and CO_2 adsorption performance of bimodal porous silica hollow spheres with amine-modified surfaces. RSC Adv. 2, 6784–6791, http://dx.doi.org/10.1039/c2ra21017g.

Zhang, H., Wu, J., Zhou, L., Zhang, D., Qi, L., 2007. Facile synthesis of monodisperse microspheres and gigantic hollow shells of mesoporous silica in mixed water–ethanol solvents. Langmuir 23 (3), 1107–1113, http://dx.doi.org/10.1021/la062542l.